

See discussions, stats, and author profiles for this publication at: <https://www.researchgate.net/publication/221745238>

# Does Shape Matter? Bioeffects of Gold Nanomaterials in a Human Skin Cell Model

ARTICLE *in* LANGMUIR · FEBRUARY 2012

Impact Factor: 4.46 · DOI: 10.1021/la204081m · Source: PubMed

CITATIONS

41

READS

78

9 AUTHORS, INCLUDING:



[Nicole Schaeublin](#)

United States Air Force

11 PUBLICATIONS 478 CITATIONS

[SEE PROFILE](#)



[A R M Nabiul Afrooz](#)

Stanford University

19 PUBLICATIONS 217 CITATIONS

[SEE PROFILE](#)



[Navid B Saleh](#)

University of Texas at Austin

68 PUBLICATIONS 3,242 CITATIONS

[SEE PROFILE](#)



[Saber M Hussain](#)

Wright-Patterson Air Force Base

137 PUBLICATIONS 8,090 CITATIONS

[SEE PROFILE](#)

dx.doi.org/10.1021/la204081m | *Langmuir* 2012, 28, 3248–3258

Table 1. Characterization of Gold Nanomaterials

nanomaterial	diameter size (nm)	length (nm)	aspect ratio	particle volume (nm <sup>3</sup> )	particle surface area (nm <sup>2</sup> )	capping molecule	Z-average particle diameter (nm)		zeta potential (mV)	
							dispersed in water	dispersed in serum free media	dispersed in water	dispersed in serum free media
Au spheres (AuNS-MPS)	20 ± 4.6	—	—	4.2 × 10 <sup>3</sup>	1.3 × 10 <sup>3</sup>	MPS	29.9 ± 0.4	514.0	−45.6 ± 1.6	−19.2 ± 1.7
Au rods (AuNR-PEG)	16.7 ± 4.3	43.8 ± 5.8	2.6	8.4 × 10 <sup>3</sup>	2.3 × 10 <sup>3</sup>	PEG-SH	17.2 ± 1.1	479.7	−13.4 ± 1.1	−7.31 ± 0.6

poly(acrylic acid) (PAA), poly(allylamine) hydrochloride (PAH), and poly(diallyldimethylammonium chloride)-poly(4-styrenesulfonic acid) (PDADMAC-PSS), or by exchanging CTAB with a less toxic ligand, such as thiol-terminal polystryrenesulfonate (PSS), mercaptohexadecanoic acid (MHDA), or poly(ethyleneglycol) (PEG).<sup>9–20</sup>

Recently, numerous studies have shown that different physical and chemical characteristics of nanoparticles play an important role in cellular uptake and cytotoxicity.<sup>21–25</sup> While many of these studies found that replacing or overcoating the CTAB on the surface of the AuNRs can reduce the cytotoxicity to cells, few have focused on specific morphological aspects of the AuNMs (such as shape) and their effects on cellular response. For example, the Arnida et al.<sup>26</sup> study comparing PEGylated and uncoated gold nanospheres (AuNS) and PEGylated AuNRs found that neither material inhibited cell proliferation of human prostate cancer PC-3 cells at 1.5 nmol/L (nM) concentrations after 88 h. In another study, Wang and colleagues<sup>16</sup> found that neither citrate-coated AuNSs nor PSS-coated AuNRs are toxic to human keratinocytes. However, the critical gap in these studies is that only cell viability was evaluated; just because a nanomaterial does not induce cell death does not automatically imply that a cell remains completely unaffected by the presence of the material. We previously demonstrated that although aluminum and aluminum oxide nanoparticles were not toxic to a lung coculture model, the aluminum nanoparticles prevented the cells from generating a normal immune response when infected with bacteria, demonstrating an adverse effect on the cells despite the absence of toxicity.<sup>27</sup> Moreover, a recent study from our lab also showed that low, nontoxic levels of gold, silver, and iron oxide all caused a disruption in EGF signaling.<sup>28</sup> Additionally, other studies in the literature have demonstrated that nanomaterials can induce immune responses and can cause inflammation.<sup>29,30</sup>

The AuNRs used in this study were pegylated to mediate the toxic effects of the CTAB. The AuNSs had a coating of 3-mercaptopropanesulfonate (MPS), which was the ligand used during synthesis. While the surface coatings are different between the AuNRs and the AuNSs, both have been shown to be biocompatible.<sup>31</sup> Therefore, the objective of this study was to provide an in depth evaluation on how differences between these two AuNMs affect cell viability, ROS, gene regulation, and immune response in human skin cells, as a model for a common dermal exposure route.

## 2. RESULTS AND DISCUSSION

**Nanoparticle Characterization.** Transmission electron microscopy (TEM) showed uniform, spherical AuNSs with a mean diameter and one standard deviation about the mean of 20 ± 4.6 nm, and AuNRs with 16.7 ± 4.3 nm × 43.8 ± 5.8 nm

average dimensions yielding an aspect ratio of 2.6 based on no less than 100 particles (Table 1 and Figure 1). Additional

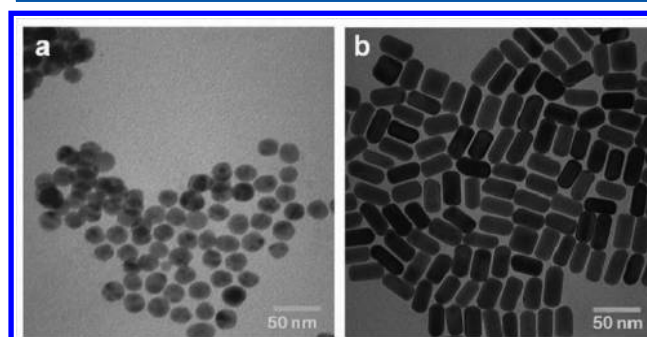


**Figure 1.** Morphology of gold nanomaterials. (a, b) Representative bright field transmission electron microscope (BF-TEM) images of Au NMs taken at 120 kV, demonstrating rod and spherical morphologies. (a) AuNS-MPS. (b) AuNR-PEG.

characterization of the AuNS-MPS, including surface chemical analysis confirmation of MPS coating, has been reported elsewhere<sup>32</sup> and is considered relevant, as the AuNS-MPS for this study was from the same batch. Dynamic light scattering (DLS) was performed to determine the agglomeration of the nanomaterials in water and in serum-free media (Table 1). Serum-free media was chosen in an attempt to keep as many parameters constant between the two AuNMs so that shape could accurately be assessed. Research has shown that the elevated amounts of protein found in serum can cause unwanted nanoparticle agglomeration due to the adsorption of serum proteins onto the surface of the nanoparticles.<sup>33–35</sup> The proteins on the nanoparticle surface are referred to as the protein corona and are heavily dependent on nanoparticle size, surface, and concentration.<sup>34,35</sup> The displacement of surface molecules with the protein corona causes a destabilization of the nanoparticle surface and results in an altered agglomeration state.<sup>33</sup> Changes in agglomeration can then lead to differences in nanoparticle uptake and cellular effects<sup>36–42</sup> and consequently masking possible shape outcomes. The DLS showed a highly stable colloidal suspension with no agglomeration of the gold nanorods and spheres in deionized water with average hydrodynamic diameters of 29.9 ± 0.4 nm for the AuNS-MPS and 17.2 ± 1.1 nm for AuNR-PEG, the mean and one standard deviation of three replicate measurements. Note that the TEM standard deviation represents the width of the size distribution, while the DLS standard deviation represents the repeatability or precision of the measurements.<sup>43</sup> However, a considerable amount of agglomeration was observed in media as the particle size increased steadily to 514 nm for AuNS-MPS and 480 nm for AuNR-PEG. This agglomeration was

caused by the high concentration of electrolytes in the media that effectively screened the electrostatic interaction between the gold nanomaterials and resulted in decreased colloidal stability.<sup>42,44–47</sup> The agglomerate structure of the spheres and rods as determined by static light scattering (SLS) showed fractal dimension  $D_f$  of  $2.57 \pm 0.4$  for the AuNS–MPS and  $1.28 \pm 0.08$  for the AuNR–PEG (Table 2), the mean and one

**Table 2. Characterization of Nanomaterial Agglomerates**

nanomaterial	primary particle size (nm)	particle size in media (nm)	fractal dimension	agglomerate shape
AuNS–MPS	$20 \pm 4.6$	514.0	$2.57 \pm 0.4$	densely packed
AuNR–PEG	$16.7 \pm 4.3$	479.7	$1.28 \pm 0.1$	loosely packed

standard deviation about the mean of three replicate measurements. The lower fractal dimension for the AuNR–PEG indicates that the agglomerates formed in media are loosely bound compared to more densely formed agglomerates in the case of AuNS–MPS, and the  $D_f$  of 2.57 suggests diffusion-limited colloidal agglomeration was driving the formation of the AuNS–MPS agglomerates.<sup>48</sup> This difference in the compactness of the agglomerates can have significant effect on particle suspension behavior and thereby their potential interaction with biological systems; this will be discussed in the subsequent section.

A note on terminology is warranted. While the classical colloidal science literature refers to these structures as “aggregates”, more recent ASTM and ISO definitions of “aggregates” refer to metal nanoparticle cores fusing together into a continuous structure, while “agglomerates” refer to assemblies of still-distinguishable primary nanoparticles. On the basis of the TEM data in Figure 2, it is most likely that

agglomerate structures were formed, and thus this term will be used for the remainder of the discussion.

Zeta ( $\zeta$ ) potential measurements for AuNMs in water and media showed that AuNS–MPS acquired significantly higher negative electrostatic potential ( $-45.6 \pm 1.6$  mV in water and  $-19.2 \pm 1.7$  mV in media) compared to AuNR–PEG ( $-13.4 \pm 1.1$  mV in water and  $-7.31 \pm 0.6$  mV in media). In general, solutions with a  $\zeta$  potential of  $<-30$  mV or  $>+30$  mV are considered to be electrostatically stable, meaning particles present in suspension will stay uniformly dispersed due to significant electrostatic repulsion.<sup>49</sup> However, a decrease in the magnitude of the  $\zeta$  potential (i.e., lower than 30 mV in magnitude) caused by electrostatic screening in the presence of salt reduces electrostatic barriers and results in agglomeration.<sup>48,50–52</sup> The findings in this study are consistent with classical colloid literature, as AuNS–MPS were found to be relatively less stable compared to its counterpart AuNR–PEG NMs (Table 1) when introduced into cell culture media. The initial colloidal stability of the AuNS–MPS is primarily due to higher electrostatic repulsion emanating from the higher  $\zeta$  potential in DI water. The charged species in the cell culture media screened the surface charges of the AuNMs and thereby caused agglomeration that is reflected in the  $\zeta$  potential and DLS results (Table 1). However, the role of the surface coating also contributes. AuNR–PEG are more stable in both DI water and cell culture media due to the steric repulsion of the bulky PEG coating on the AuNR surface. Thus, the nature of the surface coating molecule impacts how tightly bound the agglomerated structures are. Additionally, as the question of dosimetry has recently come to light, the surface area and volume of a single rod and a single sphere was calculated, assuming perfect spherical or capped cylindrical geometries and a homogeneous size distribution of only the mean values measured by TEM (see Supporting Information for more information on how these were calculated). The AuNS–MPS had a volume of  $4.2 \times 10^3$  nm<sup>3</sup> and a surface area of  $1.3 \times 10^3$  nm<sup>2</sup>, while the AuNR–PEG had a volume of  $8.4 \times 10^3$  nm<sup>3</sup> and a surface area of  $2.3 \times 10^3$  nm<sup>2</sup>. In both cases, the AuNR–PEG had a volume and surface area larger than that of the AuNS–MPS.

**Nanomaterial Uptake and Localization.** TEM was performed to ascertain the internalization and localization of the AuNMs, and energy-dispersive X-ray (EDX) analysis was performed to confirm the presence of Au. Representative TEM images verified internalization of all AuNMs into the cells after 24 h, and agglomerates of the AuNS–MPS were found in cytoplasmic vacuoles located near the cell membrane (Figure 2a–c). EDX identified the elemental composition of the agglomerates as Au in specific places within the cell as compared to no presence of Au signal in control cells (Figure 2d). The cells also contained a background signal from the copper (Cu) TEM grid.

The TEM images demonstrated different amounts of material internalization in the cells. The AuNS–MPS appeared to be readily internalized, as shown by the large cluster of particles in a vacuole (Figure 2b) compared to a few individualized rods seen in the cells treated with AuNR–PEG (Figure 2c). It was recently shown that larger and positively charged NMs (both metallic and nonmetallic) may penetrate cells in greater numbers and that spherical particles are taken up to an extent much higher than that for rods.<sup>24,25,53,54</sup> In addition, reports in the literature have revealed that exchange of PEG on the surface of nanorods reduces the interaction of

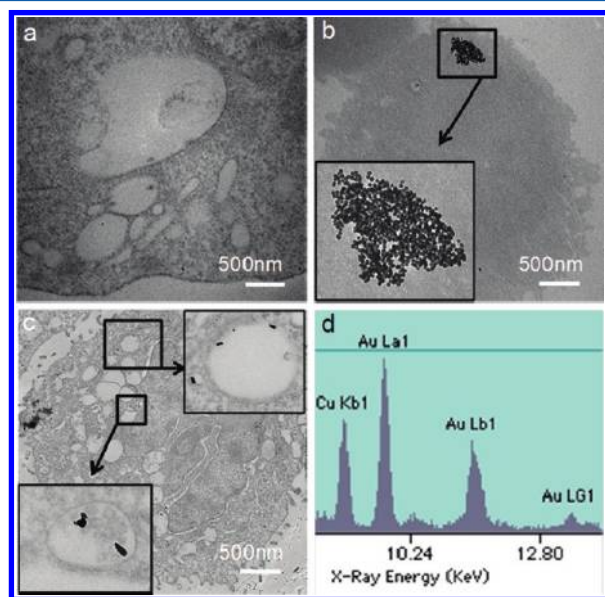


**Figure 2.** Gold nanomaterial uptake. (a–c) Bright field transmission electron microscope (BF-TEM) images of Au NMs in human skin cells. (a) Control cells, no NMs. (b) AuNS–MPS. (c) Au NR–PEG. (d) Energy-dispersive X-ray (EDX) spectra for localized elemental detection inside cells treated with AuNS–MPS.



particles with cells and leads to reduced uptake.<sup>26,55–58</sup> However, this limitation can be surmounted by using a lower molecular weight PEG.<sup>59–61</sup> The denser, longer chain length of the PEG<sub>5000</sub> used to functionalize the AuNR in this study could account for the low amount of AuNR–PEG in the cells. Furthermore, the lower fractal dimension, i.e., less-dense agglomerates or more-loosely bound structure of the AuNR–PEG, also helps in speculating the origins of the presence of individual AuNRs within the cells compared to larger clusters. The loosely bound nature of the agglomerates, likely a function of surface-coating differences, most likely induced individual rod internalization of weakly bound AuNRs from the agglomerates, highlighting how surface coating, agglomeration state, and cellular uptake are inherently entangled parameters. Nevertheless, despite the lower uptake of the AuNR–PEG, any differences in cellular response between the two AuNMs used in this study should not be discounted, as several recent studies have shown that NM uptake is not necessary to induce cellular effects.<sup>62,63</sup>

**Evaluation of Cellular Toxicity.** The MTS assay was performed to determine the effect of the AuNMs on human keratinocyte mitochondrial function. The 24 h exposure results demonstrated a difference in the toxicity of the cells treated with the AuNR–PEG as compared to untreated control cells (Figure 3). The agglomerated AuNR–PEG caused a significant

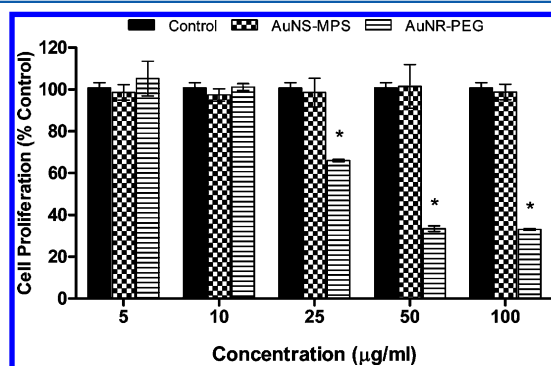


**Figure 3.** Cell proliferation following a 24 h exposure to gold nanomaterials. The AuNS–MPS did not affect cell proliferation and demonstrated growth levels comparable to that of untreated control cells as high as 100  $\mu\text{g/mL}$ . The AuNR–PEG initially did not demonstrate toxicity at low concentrations but began to inhibit cell proliferation at 25  $\mu\text{g/mL}$ . (\*Denotes significance in comparison to control values  $p < 0.05$ ).

reduction in cell viability (down to 66%) at 25  $\mu\text{g/mL}$  whereas, after treatment with the AuNS–MPS, no reduction in cell viability occurred, even at the highest dose of 100  $\mu\text{g/mL}$ . These results were in contrast to Niidome et al.<sup>19</sup> and Grabinski et al.,<sup>20</sup> both of whom found that replacing the CTAB on the surface of the AuNR with PEG reduced the cytotoxicity.<sup>19,20</sup> However, the AuNRs used in both studies had much higher aspect ratios (5.9 and 3.5, respectively), and the authors did not provide data on the agglomeration patterns; therefore, this could account for the discrepancy in cytotoxicity.

**Mitochondrial Stress.** It is known that treatment with nanomaterials and other sources of cell stress can cause cells to generate reactive oxygen species (ROS).<sup>64</sup> Therefore, generation of ROS was evaluated to determine if the AuNMs induced oxidative stress based on their shape. The ROS and remainder of the experiments were conducted with a dose of 25  $\mu\text{g/mL}$  AuNMs (as toxicity began at this dose with the AuNR–

PEG). It should be noted that the 50  $\mu\text{g/mL}$  and 100  $\mu\text{g/mL}$  doses were not tested because of the high level of toxicity at these concentrations. As only  $\sim 30\%$  of the cells were viable, it is unlikely that there would be a difference in the amount of ROS produced or change in MMP because the majority of the cells are dead.<sup>27,28,65</sup> The AuNR–PEG caused a significant amount of ROS to be formed, whereas AuNS–MPS did not (Figure 4). Additionally, because the production of ROS has

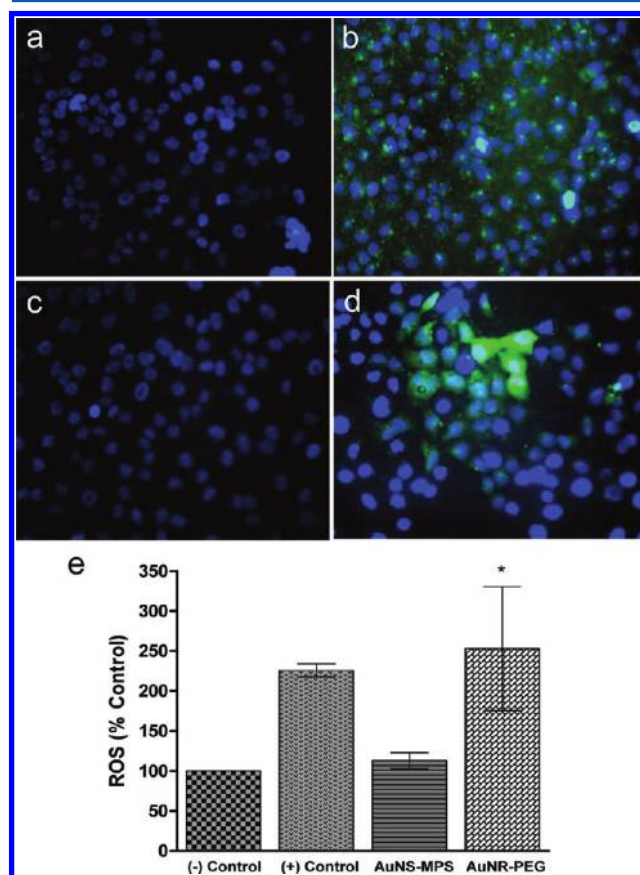


**Figure 4.** Generation of reactive oxygen species following gold nanomaterial exposure. (a) Negative control (untreated cells). (b) Positive control (*tert*-butyl hydroperoxide). (c) AuNS–MPS. (d) AuNR–PEG. The AuNS–MPS did not generate significant amounts of ROS while the AuNR–PEG displayed increased ROS when compared to the negative control. (e) Graph depicting the data shown in the images. (\*Denotes significance in comparison to negative (untreated) control values  $p < 0.05$ ).

been shown to disrupt the mitochondrial membrane potential (MMP) and indicate apoptosis,<sup>66</sup> the impact of AuNM exposure on the MMP was examined. The MMP results corroborate the ROS results, as treatment with the AuNR–PEG triggered a significant disruption in the mitochondrial membrane potential while the AuNS–MPS left the membrane intact (Figure 5). Consequently, the ROS generated from the AuNR–PEG caused the depolarization of the mitochondrial membrane. When considered together, the results of the ROS and MMP assays strengthen the conclusion that the shape, i.e., aspect ratio, of the AuNM plays a key role in cellular toxicity, with AuNR–PEG causing significantly higher stress to the cells.

**Nanomaterial Solution Purity and Surface Chemistry Control.** Although several studies have shown that both MPS and PEG are biocompatible, to ensure that there were no

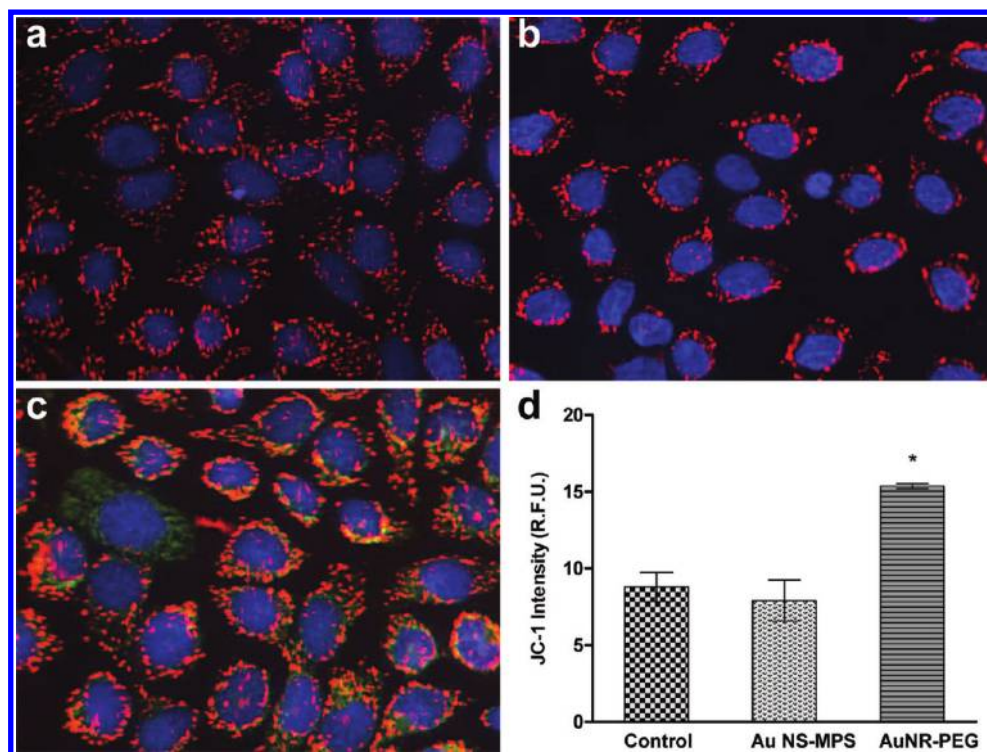


**Figure 5.** Evaluation of mitochondrial membrane potential following gold nanomaterial exposure. This assay uses JC-1, which enters healthy mitochondria, aggregates, and fluoresces red. Upon disruption of the mitochondrial membrane, the dye becomes dispersed throughout the cell and fluoresces green, indicating apoptotic cells. (a) Control cells (untreated). (b) AuNS–MPS. (c) AuNR–PEG. There was a significant amount of MMP lost after exposure to the AuNR–PEG. (d) Graph depicting the data shown in the images. (\*Denotes significance in comparison to control values  $p < 0.05$ ).

residual impurities in the samples (MPS, PEG, or CTAB), AuNMs were removed via centrifugation and cells were treated with the remaining media to ascertain toxic effects. The media from both the AuNR and AuNS stock did not generate the formation of reactive oxygen species (ROS), indicating that any changes in behavior of the cells would be linked to the AuNM morphology and not chemistry response to the molecules on the AuNM surface, whether still bound or dissociated (Figure 6a). Additionally, cellular viability was assessed on cells treated with 12 nm AuNS–PEG to further verify that the different surface chemistries were not contributing to any changes in cellular response. The results demonstrated no decrease in cellular viability after treatment with the AuNS–PEG (Figure 6b). Therefore, we can confidently conclude that the different surface molecules coating the AuNM are not dissociating nor mediating the biological response.

**Evaluation of Changes in Gene Expression.** The generation of ROS in small amounts is a common occurrence in cells and is easily neutralized by the cell antioxidant defenses, which include production of glutathione and antioxidant enzymes.<sup>67</sup> However, when significant amounts are generated (i.e., after treatment with NMs), an inflammatory response is triggered. If the inflammatory response, which is initiated through the activation of pro-inflammatory signaling cascades such as MAPK and NF $\kappa$ B, is unable to fix and repair the damage done by the ROS, then apoptotic factors (i.e., caspases) are released and cell death results.<sup>67</sup>

Upon exposure to the AuNR–PEG, the skin cells demonstrated considerable up-regulation of genes involved in cellular damage and stress (Table 3). Typically, GADD45A is transcribed following exposure to agents that can cause DNA

damage, and the expression of this gene was up-regulated 184 fold by the AuNR–PEG. Similarly, the PCNA gene, which is known to interact with GADD45A and is involved in DNA synthesis and repair, was up-regulated 9 fold. RAD23A is also important in DNA damage repair and was up-regulated 400 fold. The increase in expression of these three genes suggested that the AuNR–PEG were damaging the cells, with the production of ROS most likely causing DNA damage. Additionally, the TNFSF10 gene, an activator of the extrinsic apoptotic pathway by acting as a ligand and binding cell death receptors, was up-regulated ~4500 fold. The observed up-regulation suggested that apoptosis was initiated by these cells. This was further confirmed by the increase in expression of CASP8, which is a target for TNFSF10. Additionally, ANXA5, CASP1, and EGRI, whose expression is also associated with apoptosis, demonstrated an increase in gene expression (~20 fold). One function of CASP1 is to induce expression of certain pro-inflammatory cytokines such as IL-18 and IL-1 $\beta$ , and both of these were significantly up-regulated by the AuNR–PEG (106 fold and 21 fold, respectively). Other inflammatory genes such as IL-1 $\alpha$  and HSPA2 were also up-regulated, showing that the AuNR–PEG triggered an immune response in the cells. In contrast, the AuNS–MPS demonstrated very little change in gene expression with the down-regulation of HSP90AB1 and SERPINE1, which are both responsible for inflammation. These results are not surprising as colloidal gold is widely used in the treatment of arthritic inflammation.<sup>68</sup> The evidence collected thus far demonstrated that the AuNR–PEG caused irreparable damage to the cells and initiated an immune response, which inevitably led to cell death via the apoptotic pathway. These results are in contrast to those seen by



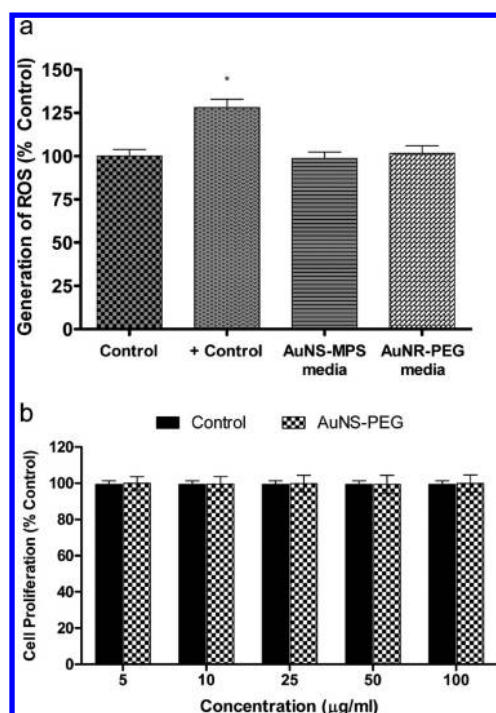


**Figure 6.** Assessment of gold nanomaterial solution purity and surface chemistry toxicity. (a) ROS generation of AuNM solution. Both the AuNS–MPS and AuNR–PEG solutions did not generate ROS as compared to the controls. (\*Denotes significance in comparison to negative control values  $p < 0.05$ ). (b) Cellular proliferation following a 24 h treatment with 12 nm AuNS–PEG. The AuNS–PEG did not cause a decrease in cellular proliferation and exhibited growth levels comparable to that of control cells as high as 100  $\mu\text{g/mL}$ .

**Table 3. Changes in Gene Expression Following Treatment with Gold Nanomaterials**

gene	function	fold regulation
AuNR–PEG		
GADD45A	DNA damage and repair	184.57
PCNA	DNA damage and repair	9.2
RAD23A	DNA damage and repair	402.08
TNFSF10	activator of immune response and apoptosis	4486.37
HSPA2	inflammation	78.87
IL18	inflammation	106.01
IL1A	inflammation	17.48
IL1B	inflammation	21.58
ANXA5	apoptosis	19.45
CASP1	apoptosis	21.63
CASP8	apoptosis	16.62
EGR1	apoptosis	19.27
AuNS–MPS		
HSP90AB1	inflammation	–10.24
SERPINE1	inflammation	–2.91

Grabinski et al.<sup>20</sup> who found that AuNR–PEG (AR 3.5) caused down-regulation of genes involved in apoptosis, growth arrest, and cellular damage. However, as stated earlier, the AR is larger for these particles, which could have an effect on the mechanism of uptake, and consequently on cellular response.

**Protein Expression Studies.** To verify whether AuNR–PEGs were causing cell death by means of apoptosis (as suggested by the real-time PCR data), protein expression was evaluated for several of the genes with increased expression. An

ELISA assay was performed to evaluate the protein level of interleukin 18 (IL-18), an inflammatory cytokine. Results of the ELISA revealed a significant amount of IL-18 protein expression after a 3 h exposure to the AuNR–PEG but not to the AuNS–MPS as compared to control cells (Figure 7).

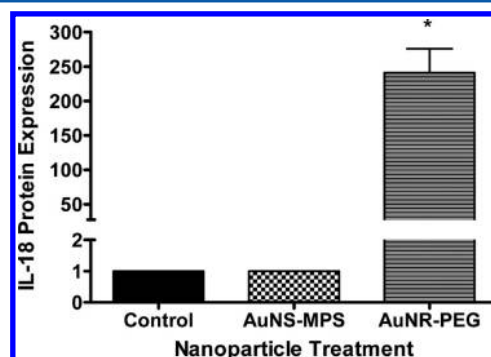


**Figure 7.** IL-18 protein expression after 6 h gold nanomaterial exposure. A significant amount of IL-18 protein was expressed after the cells were exposed to the AuNR–PEG but not the AuNS–MPS as compared to control cells. Data normalized to 1 for graphing purposes.

Additionally, immunofluorescence was performed to evaluate caspase 1 and PCNA protein expression (Figure 8). The

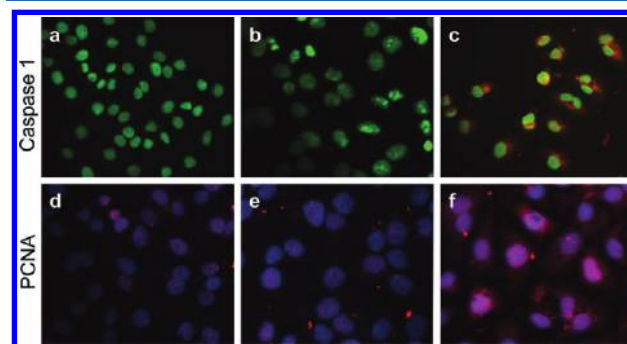


**Figure 8.** Caspase 1 and PCNA protein expression after gold nanomaterial exposure. (a–c) Caspase 1 protein expression after 24 h exposure to Au NMs. (a) Control cells, no nanomaterials. (b) AuNS–MPS. (c) AuNR–PEG. There is no caspase 1 expression in the control or the AuNS–MPS-treated cells; however, caspase 1 expression is found in the nucleus and the cytoplasm of the cells treated with AuNR–PEG. (d–f) PCNA protein expression after 24 h exposure to Au NMs. (d) Control cells, no nanomaterials. (e) AuNS–MPS. (f) AuNR–PEG. There was minimal PCNA expression found in the nuclei of the control and AuNS–MPS-treated cells, which signified that these cells were healthy and proliferating. However, there was a significant amount of PCNA found in the nuclei and the cytoplasm of the cells treated with AuNR–PEG.

caspase 1 (an enzyme that cleaves proteins, including IL-1 $\beta$  and IL-18, into active mature peptides, activates the inflammatory process and induces apoptosis) assay revealed no protein expression in the control or the AuNS–MPS treated cells (Figure 8a,b). However, protein expression was found in the nucleus and the cytoplasm of the cells treated with AuNR–PEG (Figure 8c). The PCNA protein is a cofactor of DNA polymerase delta, known to be found in small amounts in the nucleus of healthy, proliferating cells with a primary function of DNA replication and repair. Upon DNA damage, the protein is ubiquitinated and shuttled into the cytoplasm to facilitate RAD6-dependent DNA repair. Minimal PCNA expression

found in the nuclei of the control and AuNS–MPS-treated cells signified that these cells were healthy and proliferating (Figure 8d,e). However, there was a significant amount of PCNA found in the nuclei and cytoplasm of the cells treated with AuNR–PEG, suggestive of cell damage and repair (Figure 8f). These data correlate to the up-regulation of the CASP1 and PCNA genes in the real-time PCR studies and indicate that AuNR–PEG caused significant and irreparable damage to the cells while the AuNS–MPS did not, thus lending further support to our hypothesis that the shape of the AuNMs is a major factor in mitigating the cellular response to the nanomaterials.

**Mechanism of Death Study.** To verify that apoptosis was the mechanism of death for the cells exposed to the AuNR–PEG, annexin V protein expression was also evaluated (Figure 9). In healthy cells, the negatively charged phospholipid

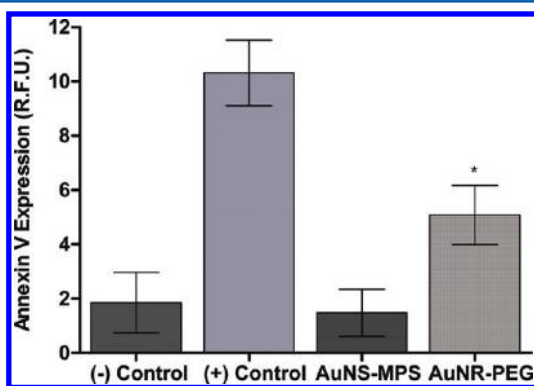


**Figure 9.** Binding of annexin V after gold nanomaterial exposure. There was significant increase in annexin V binding after exposure to AuNR–PEG as compared to the negative control (untreated cells), which confirmed that apoptosis is the mechanism of death.

phosphatidylserine (PS) is located in the cytosolic leaflet of the plasma membrane lipid bilayer. However, during apoptosis the PS is displayed on the outer face of the membrane. Annexin has a high affinity to PS in the presence of physiological concentrations of calcium ( $\text{Ca}^{2+}$ ). Given that annexin V is not cell permeable, the binding of externalized PS is selective for early apoptotic cells. There was no annexin V binding in the control cells or the cells treated with AuNS–MPS; however, there was a significant amount of the protein bound in the cells treated with the AuNR–PEG. This further signified that the AuNR–PEG caused cell death via the apoptotic pathway.

**Linking Physiochemical Properties to Mechanism of Toxicity.** The contrasting results observed between the AuNS–MPS and AuNR–PEG in the cytotoxicity, mitochondrial stress, gene, and protein studies indicated that the NM shape may play a role in the toxicity. A more difficult question to answer is why? One hypothesis is that in addition to the shape of the AuNMs, agglomerate size may play a key role in deciphering these differences. Several studies have demonstrated that cellular response to NM is dependent upon both agglomerate size and concentration.<sup>36–42</sup> While the present study showed that despite having a similar primary particle diameter and agglomerate size in media, the AuNR–PEG were found to be cytotoxic to human skin cells when compared to the AuNS–MPS. One of the major differences between these agglomerates was their fractal dimension ( $D_f$ ), which indicates a significant difference in the compactness of the agglomerates between the two materials. Additionally, the AuNR–PEG had a higher aspect ratio with a larger calculated volume and surface

area compared to that of the AuNS–MPS. Although there was not a sizable difference between the surface area of the AuNS–MPS and the AuNR–PEG ( $1.3 \times 10^3 \text{ nm}^2$  and  $2.3 \times 10^3 \text{ nm}^2$ , respectively), the AuNR–PEG had much more surface area available to interact with the cell membrane and multiple receptors. As a result, the AuNR–PEG could be causing the cell to generate more of a ROS and MMP response than when it interacts with AuNS–MPS, through multiple receptors bound on the membrane. Moreover, the shape of the AuNM may affect the mechanism of uptake in the cell and could play a key role in cellular response. This is especially possible because despite similar agglomerate sizes in the media dosed to the cells, on the basis of Figure 2, the AuNS–MPS were taken up as agglomerates while the AuNR–PEG were taken up more often as primary particles, i.e., single rods.

### 3. CONCLUSION

In conclusion, we have demonstrated that the shape is a major factor in establishing the biological response to AuNMs. Data from the viability, mitochondrial stress, gene, and protein studies attest that the AuNR–PEG had substantial detrimental effects on the cells, while exposure to the AuNS–MPS yielded distinctly different results and revealed them to be nontoxic. As a result, this study clearly indicates that the shape of the nanomaterial is a critical factor involved in mediating the cellular response to AuNMs.

### 4. EXPERIMENTAL SECTION

The identification of any commercial product or trade name does not imply endorsement or recommendation by the National Institute of Standards and Technology.

**Gold Nanoparticles.** All glassware was cleaned in aqua regia and rinsed with copious amounts of deionized water prior to synthesis. Unless otherwise specified, all chemicals were ordered from Sigma Aldrich (St. Louis, MO) of ACS reagent purity or higher and used as received. AuNSs ( $d_{\text{core}} \sim 20 \text{ nm}$ ) were synthesized through the citrate reduction of  $\text{HAuCl}_4$  (i.e., the Turkevich method). Briefly, 68 mg of  $\text{HAuCl}_4$  is dissolved in 400 mL of deionized water. Upon heating the solution to  $100^\circ\text{C}$ , 400 mg of sodium citrate hydrate (tribasic) dissolved in 20 mL of deionized water was added to the reaction solution under vigorous stirring. The solution immediately turned from yellow to clear, to purple, and finally to wine red over the course of 20 min, at which time the reaction flask was removed from the heat and cooled to room temperature. The solution was filtered through a clean 60 mL, medium porosity fritted funnel to remove any insoluble precipitates prior to further functionalization. This solution contained approximately  $2.03 \times 10^{-9} \text{ mol/L}$  (M) AuNSs, calculated assuming total reaction of the gold precursor and the measured TEM diameter. The negatively charged citrate-stabilized AuNSs were functionalized through ligand exchange reactions employing MPS (also negative in charge) in a ratio between 2:1 and 5:1 of the incoming thiol to the estimated number of available thiol “sites” on the nanoparticles in solution. The appropriate mass of thiol can be approximated using the estimated concentration of the AuNS solution, the total available surface area of the gold spheres, and the typical “footprint” of a thiol molecule on a gold surface ( $0.214 \text{ nm}^2$ ).<sup>69</sup> In this case, 2.5 mg of MPS was added to the AuNS solution and stirred for 24 h to allow completion of the ligand exchange reaction. The AuNSs were purified by three centrifugal wash cycles with deionized water.

**Synthesis of AuNRs:** Briefly, the seed solution was made by adding a freshly prepared, ice-cold  $\text{NaBH}_4$  solution (0.6 mL, 0.01 M) into a mixture solution composed of  $\text{HAuCl}_4$  (0.025 mL, 0.1 M) and CTAB (5 mL, 0.2 M). The growth solution was prepared separately by mixing  $\text{HAuCl}_4$  (0.5 mL, 0.1 M),  $\text{AgNO}_3$  (0.08 mL, 0.1 M), and CTAB (50 mL, 0.2 M) at room temperature. Next, ascorbic acid (0.55 mL, 0.1 M) was added to the growth solution as a mild reducing agent, followed by



the seed solution (0.1 mL). The color of the growth solution slowly changed from clear to violet, indicating the growth of AuNRs. The reaction condition stated above resulted in the AuNRs with aspect ratio of 2.6 (length: 43.8 nm, diameter: 16.7 nm) as shown in Figure 1b.

To prepare the AuNR-PEG, as-made AuNR solution containing CTAB (cationic) was centrifuged at 8000g for 30 min, decanted, and resuspended in water to remove excess CTAB. Next, 100  $\mu$ L of 1 mM thiol-functionalized PEG (PEG-SH) (approximate molecular weight 5000 g/mol) (neutral charge) was added to 10 mL of the 1 nM AuNR solution. The mixture was stirred for 24 h at room temperature. To ensure complete surface modification on the side as well as the end of the AuNRs, the excess PEG-SH was removed by centrifuge, and the aforementioned procedure was repeated. Finally, excess PEG-SH was removed by multiple centrifugations.

**Cell Culture.** The Army Research Lab kindly provided the human keratinocyte cell line (HaCaT).<sup>70</sup> The cells were grown in a T-75 flask with RPMI-1640 media (ATCC, Manassas, VA), supplemented with 10% (v/v) fetal bovine serum (FBS, ATCC) and 1% (w/v) penicillin/streptomycin (Sigma, St. Louis, MO) and incubated at 37 °C in a humidified incubator with 5% CO<sub>2</sub>. For AuNM exposure procedures, media was supplemented with 1% (w/v) penicillin/streptomycin but no serum.

**Nanoparticle Characterization.** To verify morphology and size, one drop of a 100  $\mu$ g/mL solution was spotted on a Formvar/carbon-coated TEM grid (EMS Diasum, Hatfield, PA) and allowed to dry. Once dried, the nanoparticles were viewed using a Philips/FEI CM200 TEM (Hillsboro, OR) at 120 kV.

**Nanoparticle Characterization in Solution.** DLS for characterization of nanoparticle size and zeta potential in solution was performed on a Malvern Instruments Zetasizer Nano-ZS instrument according to the method described by Murdock et al.<sup>71</sup>

To perform SLS measurements, AuNS-MPS and AuNR-PEG stock suspensions were diluted to obtain 25 mg/L concentrations in RPMI media in the presence of 1% (w/v) streptomycin. Fractal dimension measurement was performed using ALV-CGS/3 compact goniometer system (ALV-GmbH, Langen, Germany) equipped with a 22 mW He-Ne laser with a wavelength of 632.8 nm and coupled with an ALV/LSE-5004 digital autocorrelator (ALV-GmbH, Langen, Germany). Two milliliters of AuNM suspensions at 25 mg/L in media was added into precleaned disposable borosilicate glass vials (Fisher Scientific, Pittsburgh, PA). The rigorous cleaning procedure is described elsewhere.<sup>50,51,72</sup> This vial was kept under cell culture conditions for 24 h (exposure time in toxicity analysis) to allow the particles achieve a pseudoequilibrium agglomerate structure. Scattered light intensity was measured at 37 °C by a photon counting module operating at 1.2 A and 5 V (Perkin-Elmer, Dumberry, Canada) at scattering angles ranging from 12.5° to 100°, maintaining a 10 s time interval between consecutive readings. Triplicates measurements were performed for each scattering angle. The scattering intensity was plotted against the scattering wave vector in a log-log plot. Fractal dimensions of the AuNM agglomerates were computed using the slope of the best fit straight line using the method described elsewhere in the colloid literature.<sup>73</sup> The fractal dimension measurements were also replicated to confirm that results are reproducible.

**Cellular Uptake of Gold Nanoparticles.** HaCaT cells were processed for TEM according to Bozzola and Russell.<sup>74</sup> Briefly, the cells were seeded in six-well plates at a density of  $5 \times 10^5$  cells/well, allowed to grow overnight until ~90% confluent, and then treated with 25  $\mu$ g/mL of the different shaped AuNMs. Twenty-four hours later, the cells were removed from the plates via trypsin and centrifuged. The cell pellets were fixed in a mixture of 2% (w/v) paraformaldehyde (EMS Diasum, Hatfield, PA) and 2.5% (w/v) glutaraldehyde (EMS Diasum, Hatfield, PA) in phosphate-buffered saline (PBS) for 2 h, washed thoroughly with PBS to remove any residual aldehydes, and subsequently stained with 1% (w/v) osmium tetroxide (EMS Diasum, Hatfield, PA) for 1 h. After three additional PBS washes to remove any excess osmium, the cells were dehydrated using increasing concentrations of ethanol, with three final exchanges of 100% ethanol. The samples were then placed in 100% LR White resin (EMS Diasum,

Hatfield, PA) and cured overnight at 60 °C in BEEM capsules (EMS Diasum, Hatfield, PA) in a vacuum oven. The samples were thin-sectioned on a Leica ultramicrotome at a thickness of (50 to 100) nm, collected on Formvar/carbon-coated TEM grids, and imaged using a Philips/FEI CM200 TEM at 120 kV. Energy-dispersive X-ray (EDX) analysis was performed at various locations within the cells to confirm the presence of AuNMs with an EDAX system (Ametek, Mahwah, NJ). Controls consisted of cells not treated with nanoparticles for all experiments unless otherwise stated.

**Mitochondrial Function.** Mitochondrial function was assessed using the CellTiter 96 AQueous One Solution Assay (Promega, Madison, WI). Cells were cultured in 96-well plates with  $5 \times 10^3$  cells per well and allowed to grow at 37 °C with 5% CO<sub>2</sub> for 24 h until ~80% confluent and then treated with AuNMs at concentrations of (0 to 100)  $\mu$ g/mL. After a 24 h exposure, mitochondrial function was assessed according to the manufacturer's instructions and as described previously by Braydich-Stolle et al.<sup>75</sup> The plate was read on a SpectraMAX GeminiXS microplate reader at 490 nm to measure the absorbance. Each experiment was performed in triplicate, and the data are represented as the average of three independent trials  $\pm$  one standard deviation.

**Reactive Oxygen Species Generation.** The generation of reactive oxygen species was measured using the Image-iT Live Green Reactive Oxygen Species Detection Kit (Invitrogen, Carlsbad, CA). This kit uses a green fluorescent dye (carboxy-H<sub>2</sub>DCFDA) to measure ROS generation in live cells. Additionally, the blue-fluorescent cell permanent nucleic acid stain, Hoechst, is used to visualize the nuclei. The cells were seeded with  $5 \times 10^3$  cells per well in a 96-well black imaging plate (BD Biosciences, San Jose, CA) and allowed to grow overnight until ~80% confluent. They were then exposed to 25  $\mu$ g/mL of the AuNMs for 6 h. After 6 h, the media was removed and the cells were washed three times with PBS to eliminate any excess AuNMs that were not internalized or bound to the membrane. ROS production was induced in positive control cells by adding *tert*-butyl hydroperoxide (TBHP) for 90 min and incubating at 37 °C with 5% CO<sub>2</sub>. After 90 min, carboxy-H<sub>2</sub>DCFDA solution was added to all cells and incubated at 37 °C with 5% CO<sub>2</sub> in the dark for 30 min. After 25 min, Hoechst was added to all cells to stain the nuclei. After an additional 5 min incubation at 37 °C with 5% CO<sub>2</sub> in the dark, the solution was removed; the cells were washed three times with PBS and imaged immediately on a BD Pathway435 confocal microscope (BD Biosciences, San Jose, CA). Each experiment was performed in triplicate, and the data are represented as the average of three independent trials  $\pm$  one standard deviation.

**Mitochondrial Membrane Potential (MMP).** Mitochondrial membrane potential was evaluated using the MitE- $\psi$  Mitochondrial Permeability Detection Kit from BIOMOL (Plymouth Meeting, PA). This kit uses the cationic dye JC-1 to detect the depolarization of the mitochondrial membrane potential that occurs in apoptotic cells. The dye enters healthy mitochondria, aggregates, and fluoresces red. When the mitochondria collapses, as in apoptotic cells, the dye becomes dispersed throughout the cell, assumes its monomeric form, and fluoresces green, making it easy to distinguish between the red (nonapoptotic) cells and the green (apoptotic) cells. Additionally, Hoechst (Invitrogen, Carlsbad, CA) was added to MitE- $\psi$  solution (1:1000 dilution) to visualize the nucleus. The cells were seeded as described above (ROS assay) in a 96-well black imaging plate, allowed to grow overnight until ~80% confluent, and exposed to 25  $\mu$ g/mL of the AuNMs for 6 h. After 6 h, the media was removed, and the cells were washed three times with PBS to eliminate any excess NMs that were not internalized or bound to the membrane. Next, the cells were incubated with the MitE- $\psi$  solution for 15 min at 37 °C with 5% CO<sub>2</sub>. The solution was removed, and the cells were washed twice with PBS and imaged on a BD Pathway435 confocal microscope (BD Biosciences, San Jose, CA). Each experiment was performed in triplicate, and the data are represented as the average of three independent trials  $\pm$  one standard deviation.

**Nanomaterial Solution Purity.** The purity of the nanomaterial stock solutions was evaluated using Image-iT Live Green Reactive Oxygen Species Detection Kit (Invitrogen, Carlsbad, CA). The

AuNS–MPS and AuNR–PEG nanomaterial solutions (in serum free media) were spun down at 12 000g for 30 min. After 30 min, the supernatant was removed and recentrifuged for an additional 30 min to ensure all traces of the nanomaterials were removed from the solution. The remaining supernatant was used to treat the cells. The ROS assay was performed as described above except Hoechst was not added to stain the nucleus and the plate was read on a SpectraMAX GeminiXS microplate reader (Molecular Devices, Sunnyvale, CA) at 485 nm excitation wavelength and a 530 nm emission wavelength using the well scan setting of the instrument. Each experiment was performed in triplicate, and the data are represented as the average of three independent trials  $\pm$  one standard deviation.

**Annexin V Protein Binding.** Annexin V protein binding was evaluated using the Apoptosis and Necrosis detection kit from Enzo Life Sciences. This kit utilizes an Annexin V-Enzo Gold conjugate that fluoresces green to detect cells in the early stages of apoptosis. The cells were seeded as described above in a 96-well black imaging plate (ROS assay), allowed to grow overnight until  $\sim$ 80% confluent, and exposed to 25  $\mu$ g/mL of the AuNMs for 6 h. Additionally, 2  $\mu$ M staurosporine was added to the positive control wells for 4 h to induce apoptosis. After 6 h, they were incubated with the detection solution for 15 min at 37 °C with 5% CO<sub>2</sub>. The solution was then removed, and the cells were washed twice with PBS and imaged on a BD Pathway435 confocal microscope (BD Biosciences, San Jose, CA). Each experiment was performed in triplicate, and the data are represented as the average of three independent trials  $\pm$  one standard deviation.

**Real Time PCR.** The cells were plated in six-well plates at  $3 \times 10^5$  cells per plate and allowed to grow overnight until  $\sim$ 80% confluent. The cells were then dosed with 25  $\mu$ g/mL of the Au NMs and allowed to incubate for another 24 h. The RNA was isolated (RNeasy Mini Kit, Qiagen, Valencia, CA) and used in subsequent PCR reactions to assess cell stress and toxicity following manufacturer's instructions. The RNA was processed using SA Biosciences reagents (Frederick, MD), and the human stress and toxicity arrays (SA Biosciences) were run according to manufacturer's protocols. The data was then analyzed using SA Biosciences software. The data are represented as the average of three independent experiments  $\pm$  the standard deviation, and gene changes were only reported if  $p < 0.05$ .

**Expression of Caspase 1 and PCNA.** The cells were seeded as described above in a 96-well black imaging plate, allowed to grow overnight until  $\sim$ 80% confluent, and exposed to 25  $\mu$ g/mL of the AuNMs for 24 h. After exposure, the cells were fixed in 4% (w/v) paraformaldehyde and immunostained with a caspase-1 or PCNA primary antibody (Santa Cruz Biotechnology, Santa Cruz, CA) and an AlexaFluor 488 or 647 secondary antibody (Invitrogen, Carlsbad, CA) according to manufacturer's protocol. The nuclei were also stained with Hoechst (1:1000 dilution) (Invitrogen, Carlsbad, CA). The slides were visualized on a BD Pathway435 confocal microscope (BD Biosciences, San Jose, CA). Each experiment was performed in triplicate, and the data are represented as the average of three independent trials  $\pm$  one standard deviation.

**IL-18 Expression.** Protein expression was examined using the IL-18 ELISA assay (Invitrogen, Carlsbad, CA). The cells were plated in six-well plates at  $3 \times 10^5$  cells per plate and allowed to grow overnight until  $\sim$ 80% confluent. The cells were then dosed with 25  $\mu$ g/mL of the AuNMs and allowed to incubate for another 6 h. After 6 h, the media was collected and analyzed for protein following the manufacturer's instructions. The plate was read on a SpectraMAX GeminiXS microplate reader (Molecular Devices, Sunnyvale, CA) at 450 nm to measure the absorbance. Each experiment was performed in triplicate, and the data are represented as the average of three independent trials  $\pm$  one standard deviation.

**Image Acquisition and Data Analysis.** For the end point assays, 16 fields in each well were imaged at 20 $\times$  using the 4  $\times$  4 montage option in the BD Pathway 435 software. The ROS assay and the PCNA antibody staining used the FITC and Hoechst filters, the MitE- $\psi$  assay kit and the Apoptosis/Necrosis kit used the rhodamine, FITC, and Hoechst filters, and the Caspase 1 antibody staining used the rhodamine and Hoechst filters. Once the images were obtained, the

confocal software allowed for segmenting of the cells to measure only the fluorescent intensity within the designated portion. The images were then analyzed using the BD AttoVision v1.6 and the BD Image Data Explorer (BD Biosciences, San Jose, CA), which evaluated differences in fluorescent intensity between the samples. Each experiment was performed in triplicate, and the data are represented as the average of three independent trials  $\pm$  one standard deviation.

**Statistical Analysis.** Each experiment was performed in triplicate, and the data are represented as the average of three independent trials  $\pm$  one standard deviation. A two-way ANOVA was performed in GraphPad Prism to determine statistically significant differences in comparison to control values ( $p < 0.05$ ).

## ■ ASSOCIATED CONTENT

### § Supporting Information

Explanation of surface area calculations and a full list of genes tested in the Stress and Toxicity PCR array from SABiosciences. This material is available free of charge via the Internet at <http://pubs.acs.org/>.

## ■ AUTHOR INFORMATION

### Corresponding Author

\*Tel: 937-674-9517. Fax: 937-904-9610. E-mail: [saber.hussain@wpafb.af.mil](mailto:saber.hussain@wpafb.af.mil).

## ■ ACKNOWLEDGMENTS

The authors thank Ms. Constance Estep for help with the viability assay, Dr. Amanda Schrand for TEM imaging and EDAX, and Dr. Kristen Comfort for her assistance with critical and constructive criticism. This work was supported through AFSG funding. Ms. Schaeublin, Dr. Braydich-Stolle, and Ms. Maurer are funded through the Henry M. Jackson Foundation.

## ■ REFERENCES

- (1) Riboh, J. C.; Haes, A. J.; McFarland, A. D.; Ranjit Yonzon, C.; Van Duyne, R. P. *J. Phys. Chem. B* **2003**, *107* (8), 1772–1780.
- (2) Ghosh, P.; Han, G.; De, M.; Kim, C. K.; Rotello, V. M. *Adv. Drug Delivery Rev.* **2008**, *60* (11), 1307–1315.
- (3) Pissuwan, D.; Valenzuela, S. M.; Cortie, M. B. *Trends Biotechnol.* **2006**, *24* (2), 62–67.
- (4) Wang, Y.; Xie, X.; Wang, X.; Ku, G.; Gill, K. L.; O'Neal, D. P.; Stoica, G.; Wang, L. V. *Nano Lett.* **2004**, *4* (9), 1689–1692.
- (5) Yelin, D.; Oron, D.; Thiberge, S.; Moses, E.; Silberberg, Y. *Opt. Express* **2003**, *11* (12), 1385–1391.
- (6) Huff, T. B.; Hansen, M. N.; Zhao, Y.; Cheng, J. X.; Wei, A. *Langmuir* **2007**, *23* (4), 1596–1599.
- (7) O'Neal, D. P.; Hirsch, L. R.; Halas, N. J.; Payne, J. D.; West, J. L. *Cancer Lett.* **2004**, *209* (2), 171–176.
- (8) El-Sayed, I. H.; Huang, X.; El-Sayed, M. A. *Nano Lett.* **2005**, *5* (5), 829–834.
- (9) Cortesi, R.; Esposito, E.; Menegatti, E.; Gambari, R.; Nastruzzi, C. *Int. J. Pharm.* **1996**, *139* (1–2), 69–78.
- (10) Mirska, D.; Schirmer, K.; Funari, S. S.; Langner, A.; Dobner, B.; Brezesinski, G. *Colloids Surf., B* **2005**, *40* (1), 51–59.
- (11) Takahashi, H.; Niidome, Y.; Niidome, T.; Kaneko, K.; Kawasaki, H.; Yamada, S. *Langmuir* **2005**, *22* (1), 2–5.
- (12) Connor, E.; Mwamuka, J.; Gole, A.; Murphy, C.; Wyatt, M. *Small* **2005**, *1* (3), 325–327.
- (13) Alkhalany, A. M.; Nagaria, P. K.; Hexel, C. R.; Shaw, T. J.; Murphy, C. J.; Wyatt, M. D. *Small* **2009**, *5* (6), 701–708.
- (14) Hauck, T.; Ghazani, A.; Chan, W. *Small* **2008**, *4* (1), 153–159.
- (15) Leonov, A. P.; Zheng, J.; Clogston, J. D.; Stern, S. T.; Patri, A. K.; Wei, A. *ACS Nano* **2008**, *2* (12), 2481–2488.
- (16) Wang, S.; Lu, W.; Tovmachenko, O.; Rai, U. S.; Yu, H.; Ray, P. C. *Chem. Phys. Lett.* **2008**, *463* (1–3), 145–149.

- (17) Parab, H. J.; Chen, H. M.; Lai, T. C.; Huang, J. H.; Chen, P. H.; Liu, R. S.; Hsiao, M.; Chen, C. H.; Tsai, D. P.; Hwu, Y. K. *J. Phys. Chem. C* **2009**, *113* (18), 7574–7578.
- (18) Boca, S. C.; Astilean, S. *Nanotechnology* **2010**, *21* (23), 235601.
- (19) Niidome, T.; Yamagata, M.; Okamoto, Y.; Akiyama, Y.; Takahashi, H.; Kawano, T.; Katayama, Y.; Niidome, Y. *J. Controlled Release* **2006**, *114* (3), 343–347.
- (20) Grabinski, C. M.; Schaeublin, N. M.; Wijaya, A.; D'Couto, H.; Baxamusa, S. A.; Hamad-Schifferli, K.; Hussain, S. M. *ACS Nano* **2011**, *5* (4), 2870–2879.
- (21) Hussain, S. M.; Braydich-Stolle, L. K.; Schrand, A. M.; Murdock, R. C.; Yu, K. O.; Mattie, D. M.; Schlager, J. J.; Terrones, M. *Adv. Mater.* **2009**, *21* (16), 1549–1559.
- (22) Carlson, C.; Hussain, S. M.; Schrand, A. M.; Braydich-Stolle, K.; Hess, K. L.; Jones, R. L.; Schlager, J. J. *J. Phys. Chem. B* **2008**, *112* (43), 13608–13619.
- (23) Braydich-Stolle, L.; Schaeublin, N.; Murdock, R.; Jiang, J.; Biswas, P.; Schlager, J.; Hussain, S. *J. Nano Res.* **2009**, *11* (6), 1361–1374.
- (24) Chithrani, B. D.; Ghazani, A. A.; Chan, W. C. *Nano Lett.* **2006**, *6* (4), 662–668.
- (25) Chithrani, B. D.; Chan, W. C. *Nano Lett.* **2007**, *7* (6), 1542–1550.
- (26) Arnida; Malugin, A.; Ghandehari, H. *J. Appl. Toxicol.* **2010**, *30* (3), 212–217.
- (27) Braydich-Stolle, L. K.; Speshock, J. L.; Castle, A.; Smith, M.; Murdock, R. C.; Hussain, S. M. *ACS Nano* **2010**, *4* (7), 3661–3670.
- (28) Comfort, K. K.; Maurer, E. I.; Braydich-Stolle, L. K.; Hussain, S. M. *ACS Nano* **2011**, *5* (12), 10000–10008.
- (29) Hutter, E.; Boridy, S.; Labrecque, S.; Lalancette-Hebert, M.; Kriz, J.; Winnik, F. M.; Maysinger, D. *ACS Nano* **2010**, *4* (5), 2595–2606.
- (30) Dobrovolskaia, M. A.; Mcneil, S. E. *Nat. Nanotechnol.* **2007**, *2*, 469–478.
- (31) Smetana, A. B.; Klabunde, K. J.; Marchin, G. R.; Sorensen, C. M. *Langmuir* **2008**, *24* (14), 7457–7464.
- (32) MacCuspie, R. I.; Elsen, A. M.; Diamanti, S. J.; Patton, S. T.; Altfeder, I.; Jacobs, J. D.; Voevodin, A. A.; Vaia, R. A. *Appl. Organomet. Chem.* **2010**, *24* (8), 590–599.
- (33) Limbach, L. K.; Li, Y. C.; Grass, R. N.; Brunner, T. J.; Hintermann, M. A.; Muller, M.; Gunther, D.; Stark, W. J. *Environ. Sci. Technol.* **2005**, *39*, 9370–9376.
- (34) Lundqvist, M.; Stigler, J.; Elia, G.; Lynch, I.; Cedervall, T.; Dawson, K. A. *Proc. Natl. Acad. Sci. U.S.A.* **2008**, *105*, 14265–14270.
- (35) Cedervall, T.; Lynch, I.; Lindman, S.; Berggård, T.; Thulin, E.; Nilsson, H.; Dawson, K. A.; Linse, S. *Proc. Natl. Acad. Sci. U.S.A.* **2007**, *104*, 2050–2055.
- (36) Albanese, A.; Chan, W. C. *ACS Nano* **2011**, *5* (7), 5478–5489.
- (37) Qiu, Y.; Liu, Y.; Wang, L. M.; Xu, L. G.; Bai, R.; Ji, Y. L.; Wu, X. C.; Zhao, Y. L.; Li, Y. F.; Chen, C. Y. *Biomaterials* **2010**, *31*, 7606–7619.
- (38) Lacerda, S. H.; Park, J. J.; Meuse, C.; Pristinski, D.; Becker, M. L.; Karim, A.; Douglas, J. F. *ACS Nano* **2010**, *4*, 365–379.
- (39) Rausch, K.; Reuter, A.; Fischer, K.; Schmidt, M. *Biomacromolecules* **2010**, *11*, 2836–2839.
- (40) Maiorano, G.; Sabella, S.; Sorce, B.; Brunetti, V.; Malvindi, M. A.; Cingolani, R.; Pompa, P. P. *ACS Nano* **2010**, *4*, 7481–7491.
- (41) Kim, D.; El-Shall, H.; Dennis, D.; Morey, T. *Colloids Surf., B* **2005**, *40*, 83–91.
- (42) Zook, J. M.; MacCuspie, R. I.; Locascio, L. E.; Halter, M. D.; Elliott, J. T. *Nanotoxicology* **2011**, *5* (4), 517–530.
- (43) MacCuspie, R. I.; Rogers, K.; Patra, M.; Suo, Z.; Allen, A. J.; Martin, M. N.; Hackley, V. A. *J. Environ. Monit.* **2011**, *13*, 1212.
- (44) Phenrat, T.; Long, T. C.; Lowry, G. V.; Veronesi, B. *Environ. Sci. Technol.* **2009**, *43*, 195–200.
- (45) Long, T. C.; Saleh, N.; Tilton, R. D.; Lowry, G. V.; Veronesi, B. *Environ. Sci. Technol.* **2006**, *40*, 4346–4352.
- (46) Long, T. C.; Tajuba, J.; Sama, P.; Saleh, N.; Swartz, C.; Parker, J.; Hester, S.; Lowry, G. V.; Veronesi, B. *Environ. Health Perspect.* **2007**, *115*, 1631–1637.
- (47) Veronesi, B.; Tajuba, J.; Saleh, N.; Ward, W.; Hester, S.; Carter, J.; Lowry, G. V. *Nanotoxicology* **2008**, *2*, 130–143.
- (48) Lin, M. Y.; Lindsay, H. M.; Weitz, D. A.; Ball, R. C.; Klein, R.; Meakin, P. *Nature* **1989**, *339*, 360–362.
- (49) Hunter, R. J. *Introduction to Modern Colloid Science*; Oxford University Press: New York, 1993; p 229.
- (50) Saleh, N. B.; Pfefferle, L. D.; Elimelech, M. *Environ. Sci. Technol.* **2008**, *42*, 7963–7969.
- (51) Saleh, N. B.; Pfefferle, L. D.; Elimelech, M. *Environ. Sci. Technol.* **2010**, *44*, 2412–2418.
- (52) Saleh, N.; Kim, H. J.; Phenrat, T.; Matyjaszewski, K.; Tilton, R. D.; Lowry, G. V. *Environ. Sci. Technol.* **2008**, *42*, 3349–3355.
- (53) Orr, G.; Panther, D. J.; Phillips, J. L.; Tarasevich, B. J.; Dohnalkova, A.; Hu, D.; Teegarden, J. G.; Pounds, J. G. *ACS Nano* **2007**, *1* (5), 463–475.
- (54) Gratton, S. E. A.; Ropp, P. A.; Pohlhaus, P. D.; Luft, J. C.; Madden, V. J.; Napier, M. E.; DeSimone, J. M. *Proc. Natl. Acad. Sci. U.S.A.* **2008**, *105* (33), 11613–11618.
- (55) Hamblin, M. R.; Miller, J. L.; Rizvi, I.; Loew, H. G.; Hasan, T. *Br. J. Cancer* **2003**, *89* (5), 937–943.
- (56) Gref, R.; Minamitake, Y.; Peracchia, M. T.; Trubetskoy, V.; Torchilin, V.; Langer, R. *Science* **1994**, *263*, 1600–1603.
- (57) Mosqueira, V. C.; Legrand, P.; Gref, R.; Heurtault, B.; Appel, M.; Barratt, G. *J. Drug Target* **1999**, *7*, 65–78.
- (58) Mosqueira, V. C.; Legrand, P.; Morgat, J. L.; Vert, M.; Mysiakine, E.; Gref, R.; et al. *Pharm. Res.* **2001**, *18*, 1411–1419.
- (59) Etame, A. B.; Smith, C.; Chan, W. C. W.; Rutka, J. T. *Nanomedicine* **2011**, *7*, 992–1000.
- (60) Lipka, J.; Semmler-Behnke, M.; Sperling, R. A.; Wenk, A.; Takenaka, S.; Schleh, C.; Kissel, T.; Parak, W. J.; Kreyling, W. G. *Biomaterials* **2010**, *31*, 6574–6581.
- (61) Cruz, L. J.; Tacke, P. J.; Fokkink, R.; Figdor, C. G. *Biomaterials* **2011**, *32*, 6791–6803.
- (62) Bhabra, G.; Sood, A.; Fisher, B.; Cartwright, L.; Saunders, M.; Evans, W. H.; Surprenant, A.; Lopez-Castejon, G.; Mann, S.; Davis, S. A.; Hails, L. A.; Ingham, E.; Verkade, P.; Lane, J.; Heesom, K.; Newson, R.; Case, C. P. *Nat. Nanotechnol.* **2009**, *4*, 876–883.
- (63) Sood, A.; Salih, S.; Roh, D.; Lacharme-Lora, L.; Parry, M.; Hardiman, B.; Keehan, R.; Grummer, R.; Winterhager, E.; Gokhale, P. J.; Andrews, P. W.; Abbott, C.; Forbes, K.; Westwood, M.; Aplin, J. D.; Ingham, E.; Papageorgiou, I.; Berry, M.; Liu, J.; Dick, A. D.; Garland, R. J.; Williams, N.; Singh, R.; Simon, A. K.; M. Lewis, M.; J. Ham, J.; L. Roger, L.; D. M. Baird, D. M.; L. A. Crompton, L. A.; M. A. Caldwell, M. A.; Swallow, H.; Birch-Machin, M.; Lopez-Castejon, G.; Randall, A.; Lin, H.; Suleiman, M.-S.; Evans, W. H.; Newson, R.; Case, C. P. *Nat. Nanotechnol.* **2011**, *6*, 824–833.
- (64) Nel, A.; Xia, T.; Mädler, L.; Li, N. *Science* **2006**, *311* (5761), 622–627.
- (65) Schaeublin, N. M.; Braydich-Stolle, L. K.; Schrand, A. M.; Miller, J. M.; Hutchison, J.; Schlager, J. J.; Hussain, S. M. *Nanoscale* **2011**, *3* (2), 410–420.
- (66) Green, D. R.; Reed, J. C. *Science* **1998**, *281* (5381), 1309–1312.
- (67) Halliwell, B. *Gutteridge, J. M. C. Free Radicals in Biology and Medicine*; Oxford University Press: Oxford, UK, 1999.
- (68) Boisselier, E.; Astruc, D. *Chem. Soc. Rev.* **2009**, *38* (6), 1759–1782.
- (69) Jazdzinsky, P. D.; Calero, G.; Ackerson, C. J.; Bushnell, D. A.; Kornberg, R. D. *Science* **2007**, *318*, 430–433.
- (70) Boukamp, P.; Petrussevska, R. T.; Breitkreutz, D.; Hornung, J.; Markham, A.; Fusenig, N. E. *J. Cell Biol.* **1988**, *106* (3), 761–771.
- (71) Murdock, R. C.; Braydich-Stolle, L.; Schrand, A. M.; Schlager, J. J.; Hussain, S. M. *Toxicol. Sci.* **2008**, *101* (2), 239–253.
- (72) Surdo, E. M.; Khan, I. A.; Choudhury, A. A.; Saleh, N. B.; Arnold, W. A. *J. Hazard. Mater.* **2011**, *188* (1–3), 334–340.
- (73) Kim, A. Y.; Berg, J. C. *Langmuir* **2000**, *16*, 2101–2104.



- (74) Bozzola, J. J.; Russell, L. D. *Electron Microscopy. Principles and Techniques for Biologists*; Jones and Bartlett Publishers: Boston, MA, 1992; pp 16–37.
- (75) Braydich-Stolle, L.; Hussain, S.; Schlager, J. J.; Hofmann, M. C. *Toxicol. Sci.* **2005**, *88* (2), 412–419.